# Improving Light Harvesting in Dye-Sensitized Solar Cells Using Hybrid Bimetallic Nanostructures

Holly F. Zarick,[†] William R. Erwin,[†] Abdelaziz Boulesbaa,[‡] Olivia K. Hurd,[§] Joseph A. Webb,[†] Alexander A. Puretzky,[‡] David B. Geohegan,[‡] and Rizia Bardhan*[,†]

Departments of [†]Chemical and Biomolecular Engineering and [§]Mechanical Engineering, Vanderbilt University, Nashville, Tennessee 37235, United States

[‡]Center for Nanophase Materials Sciences, Oak Ridge National Laboratory, Oak Ridge, Tennessee 37831, United States

S Supporting Information
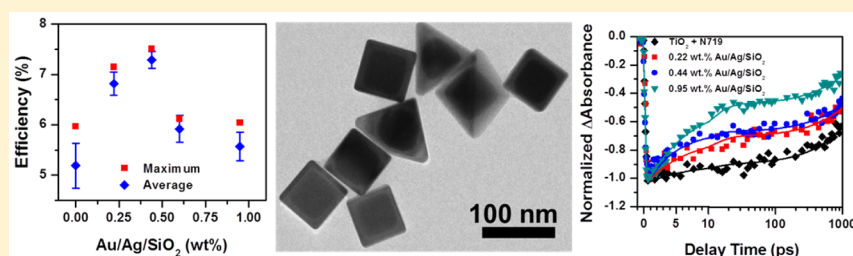
ABSTRACT: In this work we demonstrate improved light trapping in dye-sensitized solar cells (DSSCs) with hybrid bimetallic gold core/silver shell nanostructures. Silica-coated bimetallic nanostructures (Au/Ag/SiO$_2$ NSs) integrated in the active layer of DSSCs resulted in 7.51% power conversion efficiency relative to 5.97% for reference DSSCs, giving rise to 26% enhancement in device performance. DSSC efficiencies were governed by the particle density of Au/Ag/SiO$_2$ NSs with best performing devices utilizing only 0.44 wt % of nanostructures. We performed transient absorption spectroscopy of DSSCs with variable concentrations of Au/Ag/SiO$_2$ NSs and observed an increase in amplitude and decrease in lifetime with increasing particle density relative to reference. We attributed this trend to plasmon resonant energy transfer and population of the singlet excited states of the sensitizer molecules at the optimum concentration of NSs promoting enhanced exciton generation and rapid charge transfer into TiO$_2$.

KEYWORDS: dye-sensitized solar cell, plasmon-enhanced solar cell, bimetallic nanostructures, transient absorption spectroscopy, electron dynamics

Dye-sensitized solar cells (DSSCs), a class of mesoporous solar device, have evolved in the past two decades as an inexpensive alternative to silicon photovoltaics; however, low efficiencies of 8−10% have remained a major roadblock to commercialization in DSSCs.[1−3] Recently, metal nanostructures have emerged as a transformational approach to augment light harvesting in solar cells, giving rise to enhanced optical absorption, carrier generation, and improved efficiency.[4−10] Through small additions of metal nanostructures (<2 wt %), the active material required to achieve high efficiency solar conversion can be drastically reduced,[11] enabling thin film architectures compatible with scalable manufacturing routes. Upon illumination, metal nanostructures with subwavelength dimensions couple incident photons to conduction electrons, giving rise to localized surface plasmon resonances (LSPR).[12,13] By altering the shape, size, and composition of metal nanostructures, LSPRs can be manipulated to give rise to unique optical characteristics that can be harnessed for several technological applications from spectroscopy[14−16] to nano-medicine[17−19] to photovoltaics.[20−22]

Plasmonic enhancement in DSSCs is achieved by four possible mechanisms: (*i*) Far-field coupling of scattered light:

light incident on metal nanostructures with a sufficiently high albedo (ratio of total scattered light to extinction) is scattered into the far-field, reaching distances up to 10× the geometrical area[22,23] and is ultimately reabsorbed by the sensitizer.[24,25] In addition, nanostructures can also capture solar photons not absorbed by the sensitizer, which is achieved by tuning the plasmon resonance to wavelengths complementary to the sensitizers absorption.[26,27] Both processes increase the total light harvested by the solar cell. (*ii*) Near-field coupling of electromagnetic fields: nanostructures function as antennas concentrating incident light on the metal surface and generating intense near-fields, which can be orders of magnitude higher than incident light. Proximal sensitizers couple with the strong near-fields, and the enhanced photon flux increases the total absorption cross-section of the solar cell. (*iii*) Plasmon resonance energy transfer (PRET): PRET is similar to Förster resonance energy transfer, where the LSPR dipole replaces the fluorescent molecule. In this nonradiative process, energy from
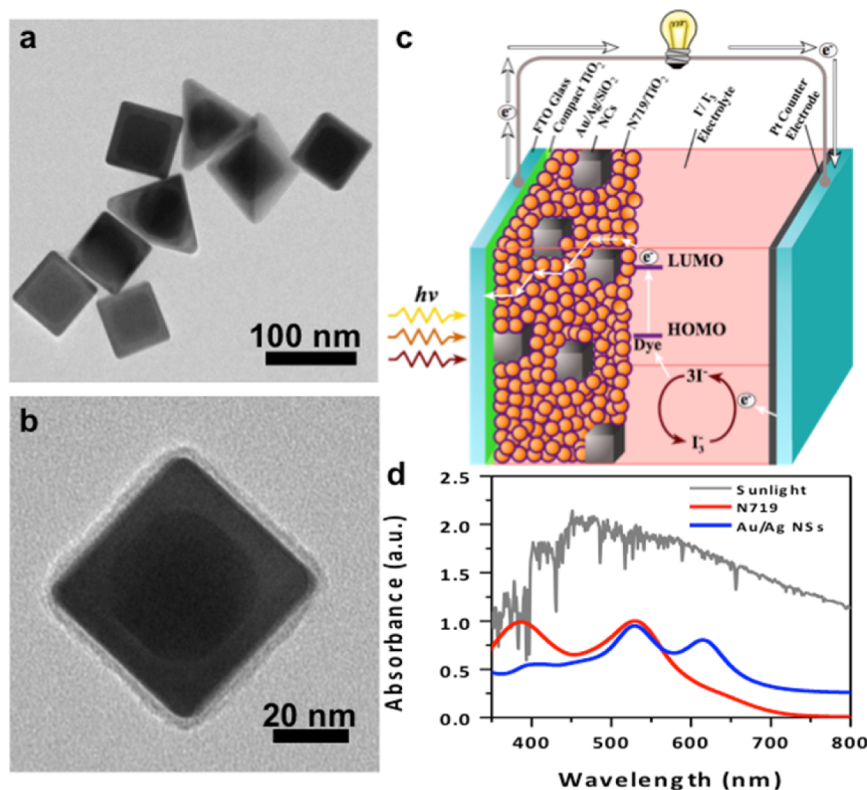
Figure 1. (a) Low-magnification TEM image of Au/Ag NSs and (b) high magnification image after silica coating the nanostructures. (c) Schematic of operation of plasmon-enhanced DSSCs showing bimetallic nanostructures embedded within the N719-sensitized mesoporous TiO₂ layer with an I⁻/I₃⁻ liquid electrolyte. (d) Normalized extinction spectrum of Au/Ag NSs in aqueous media and normalized absorption spectrum of N719 compared to the solar irradiance spectrum, which has been offset for clarity, of ASTM G173-03 reference (AM 1.5).

the metal nanostructures contained in the localized plasmonic oscillations is transferred to the semiconductor or vicinal sensitizer inducing charge separation and e⁻/h⁺ pair generation. Unlike the transfer of "hot" electrons, which depends on band alignment of semiconductor with metal Fermi level, the dipole−dipole energy transfer mechanism of PRET is not limited by band alignment and charge equilibration. PRET is also unaffected by any insulating interlayer, such as SiO₂ between the metal and semiconductor.[28,29] (iv) "Hot" electron transfer: if a plasmon is neither scattered nor undergoes PRET, then it is absorbed by the metal and decays via energetic relaxation generating e⁻/h⁺ pairs. These photoexcited electrons undergo electron−electron scattering giving rise to a "hot" electron distribution. These energetic electrons can gain enough energy to overcome the Schottky barrier at the metal/semiconductor junction and rapidly transfer (at picosecond time scales) into the semiconductor conduction band, amplifying the number of carriers available for photocurrent generation.[23,30,31] Unlike PRET, any insulating spacer separating the metal and semiconductor will block hot electrons from transferring unless the spacer thickness is less than the electron tunneling barrier of the insulator (<3 nm for SiO₂).

While plasmonic enhancement of DSSCs has largely focused on monometallic spherical nanostructures,[32−36] in this study we demonstrate the use of Au/Ag/SiO₂ bimetallic core/shell/shell nanostructures with controlled morphology and composition, tailored to maximize light harvesting in DSSCs. These bimetallic nanostructures have several advantages: (i) they possess multipolar plasmon resonances due to the use of dual metals resulting in broadband capture of solar light specifically at longer wavelengths where the dye sensitizer has poor light absorption,[37] (ii) they have well-defined nonspherical geometries, which give rise to intense near-field enhancements localized at the edges and corners of the nanostructures facilitating superior light harvesting abilities, (iii) the use of Ag can potentially reduce Ohmic losses compared to Au alone, resulting in enhanced radiative damping and strong light scattering,[38] (iv) the presence of dual metals and nonspherical geometry promotes 10× more light scattering relative to monometallic nanoparticles improving the total light absorbed in the active layer, and (v) they have a tunable core−shell architecture that allows modulation of optical and electronic properties with minimal alterations of overall size.[12]

In this work we have enhanced the performance of standard DSSCs by integrating Au/Ag/SiO₂ nanostructures (NSs) in the mesoporous layer. By varying the particle density, we find a systematic dependence of nanostructure concentration on device efficiency. While previous studies on plasmonic enhancement of DSSCs have utilized ∼0.6−3 wt % of nanoparticles,[20,36,39,40] here only 0.44 wt % Au/Ag/SiO₂ NSs in the photoanodes resulted in a 26% enhancement in the power conversion efficiency (PCE) of the device, largely attributed to an improvement in short circuit current density. The incident photon to charge conversion efficiency (IPCE) and absorbance of the devices demonstrate that enhanced light harvesting is driven by direct coupling of nanostructure plasmons with the sensitizer, N719 (di-tetrabutylammonium cis-bis(isothiocyanato)bis(2,2-bipyridyl-4,4-dicarboxylato)-ruthenium(II)) dye. In addition, IPCE and absorbance provide evidence for broadband light capture at wavelengths beyond 550 nm, where N719 does not absorb, attributable to the multipolar plasmon resonances of the nanostructures. We also

performed pump–probe transient absorption spectroscopy (TAS) on the reference and plasmon enhanced DSSCs to understand the fundamental underpinnings of exciton generation and electron injection lifetimes in DSSCs in the presence of the nanostructures. *To our knowledge, this is the first study that examines TAS of plasmon-enhanced DSSCs as a function of particle density.* We observed a decrease in lifetimes obtained from TAS with increasing concentration of bimetallic nanostructures in the devices, which we have attributed to a combination of enhanced exciton generation and rapid injection of electrons into the TiO_2 conduction band.

Bimetallic Au/Ag core/shell nanostructures (Au/Ag-NSs) were synthesized following our previously reported seed-mediated growth process.[11] Initially, Au nanocrystal (NC) cores of ~45 nm edge length were synthesized utilizing cetyltrimethylammonium bromide (CTAB) as a shape directing agent in aqueous media. Subsequently, Au NC cores were transferred into a growth solution with cetyltrimethylammonium chloride (CTAC) ligands, Ag^+ ions, KBr, and ascorbic acid and were reacted to form a thin Ag shell around the Au cores (Figure 1a). Sharp edges and corners enable strong electromagnetic fields; therefore, to promote such growth in the Ag layer, the reaction was carried out at an elevated temperature. We demonstrated in our previous work that by increasing the reaction temperature, Ag growth is preferentially accelerated along the [100] and [111] crystal planes, resulting in more defined edges and corners than those attained in the Au NC cores.[11] These shapes are governed by the shape of the Au core, where rounded-edge Au nanocubes give rise to bimetallic nanocubes and truncated Au nanocube cores generate bimetallic nanopyramids. While shape impurity is unavoidable during this seed-mediated growth process,[41−43] this mixture of shapes is advantageous in our DSSC in capturing broadband solar light, as discussed below.

Prior to incorporation into the photoanodes of the devices, the Au/Ag-NSs were coated with a thin (~5 nm) layer of silica,[23] giving rise to Au/Ag/SiO$_2$ nanostructures (Figure 1b). The silica layer serves several purposes, including (*i*) ensuring electrical isolation to minimize electron recombination on the metal surface, (*ii*) minimizing Ostwald ripening during annealing of the photoanode at 500 °C, which is necessary to convert TiO_2 to anatase phase, (*iii*) the oxides of silica provide similar chemical functionality as the TiO_2, promoting infiltration and attachment of dye throughout the active layer, and (*iv*) providing resistance to degradation in the presence of the iodide/triiodide (I^-/I_3^-) corrosive liquid electrolyte. The ~5 nm silica layer is sufficient to provide thermal and electrochemical stability[35,44,45] without detrimentally damping the plasmon; thicker layers of silica (>10 nm) shield the electron oscillation on the metal, resulting in a decrease in nanoparticle near-fields. The thin spacer layer enables enhanced near-field coupling between Au/Ag/SiO$_2$ NSs and N719 dye, promoting plasmon enhanced dye-excitation, which is controlled by the metal–molecule distance.[33,46]

The silica-coated Au/Ag-NSs were purified, concentrated, and mixed with the nanocrystalline TiO_2 paste to form a homogeneous mixture before depositing on FTO glass by the doctor-blading technique, which yielded a ~10 μm thick active layer (Figure S1). The reference and bimetallic nanostructure embedded photoanodes were sensitized with N719 dye and integrated with a counter electrode consisting of a thin layer of Pt on FTO glass. The two electrodes were heat sealed together with a low-temperature thermoplastic sealant and injected with

I^-/I_3^- based liquid electrolyte. A schematic representation of DSSC architecture and device operation is depicted in Figure 1c. In a DSSC, upon light exposure, electrons (e^-) are excited from the HOMO to the LUMO band of the dye and are rapidly injected into the conduction band of the TiO_2, subsequently traveling through the conductive electrode via the external circuit to the counterelectrode. The I^-/I_3^- redox couple promotes shuttling of e^-, reducing I_3^- to I^- at the counterelectrode. The oxidized dye then replenishes the e^- lost during photoexcitation by oxidizing I^- to I_3^-.[47] The homogeneous distribution of the Au/Ag/SiO$_2$ NSs throughout the mesoporous TiO_2 layer increases proximity to N719 molecules, maximizing near-field coupling with the sensitizer and total light harvested in the active layer while minimizing any detrimental effects to the redox processes necessary for DSSC operation.

The multipolar plasmon resonances of Au/Ag-NSs not only have good overlap with the optical absorption of N719 centered at 390 and 530 nm, but also capture broadband solar light (Figure 1d). The nanostructures exhibit two dipolar resonances at ~535 and 615 nm attributed to the Au/Ag nanocubes and nanopyramids, respectively, as described in our previous work.[11] The nanostructures also demonstrate a broad mode at 400 nm assigned to the interband transition of Ag and higher order modes associated with the nanocube corners.[11] The direct overlap of the plasmon resonances of Au/Ag-NSs with N719 absorption enables strong metal–molecule coupling, allowing enhanced light trapping.[48,49] In addition, the 615 nm resonance attributed to the Au/Ag nanopyramids extends the light-harvesting ability of the plasmonic DSSCs to spectral regions where N719 does not absorb, therefore, enabling broadband solar light capture.

We performed finite difference time domain (FDTD) simulations on single particles in aqueous media to understand the advantages of bimetallic composition and nonspherical geometries. Calculated electromagnetic (EM) field intensity enhancements of a rounded-edge Au nanocube, Au/Ag nanocube, Au/Ag nanopyramid, and Au/Ag nanosphere at their LSPR frequency are shown in Figure 2a−d. Additional simulations that further decouple the impact of the morphology and composition can be found in Figure S2. Compared with the Au nanocube (Figure 2a), the Au/Ag nanocube (Figure 2b) has a stronger field enhancement attributable to the sharp corners of the Ag shell, presence of Ag that has low Ohmic losses and strong light scattering, and the synergistic plasmonic coupling between the Au core and its Ag shell.[11,50−52] While Au is more electronegative than Ag, Ag has a higher electron conductivity; the synergistic combination of the two metals in a core/shell architecture improves their electronic properties. The sharp edges and corners of the Au/Ag nanocube (Figure 2b) and Au/Ag nanopyramid (Figure 2c) also give rise to an intense nanoantenna effect and a quasistatic lightning-rod effect,[12,53−55] making these geometries ideally suited for light concentration in DSSCs. Further, these edges also provide superior performance over bimetallic nanospheres (Figure 2d) in the augmentation of light harvesting capabilities of N719 sensitizer. Corresponding calculated normalized scattering cross sections (Q_{scat}) of each of these nanostructures (Figure 2e) demonstrate that the addition of the silver shell increases the light scattering ability of the Au/Ag nanocube to nearly 10× greater than that of the Au nanocube. In addition, the anisotropic bimetallic geometries have 2−3× higher light scattering relative to the
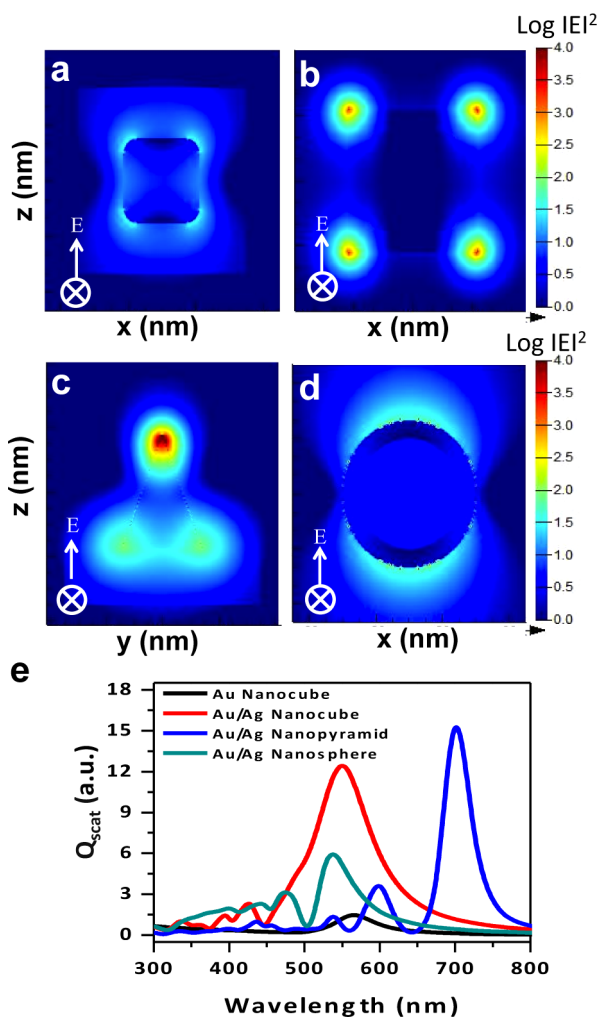
Figure 2. Electromagnetic intensity profiles, $\langle E^2/E_0^2 \rangle$ with a scale bar of $10^0 - 10^4$, of (a) a rounded edge Au nanocube, and bimetallic (b) nanocube, (c) nanopyramid, and (d) nanosphere simulated in aqueous media. Corresponding calculated scattering cross sections (area normalized) for all simulated nanostructures are shown in (e).

Figure 3. (a) Optical absorption spectra of N719-sensitized mesoporous TiO_2 with varied particle density of $Au/Ag/SiO_2$ nanostructures embedded in the photoanodes. (b) Corresponding current density spectra of the devices, and (c) % IPCE of the same devices as a function of excitation wavelength. Parts (a)−(c) are color coordinated with the legend provided in (a).

Au/Ag nanosphere, allowing augmented light trapping via an increased optical path length.

The light-harvesting capabilities of the $Au/Ag/SiO_2$ NSs were investigated by incorporating them into the photoanodes of DSSCs and comparing to reference devices (no plasmonic nanostructures). The particle density of incorporated nanostructures within the mesoporous TiO_2 matrix was varied between 0.22 and 0.95 wt % to find the optimal range for plasmonic enhancement. The absorption spectra of the plasmon-enhanced photoanodes, when compared to the reference, shows a gradual increase across the entire visible spectrum with increasing particle density from 400−550 and >600 nm overlapping with the plasmon resonance peaks of $Au/Ag/SiO_2$ NSs (Figure 3a). By normalizing the absorbance of the plasmon-enhanced devices to the reference (0 wt %), the relative enhancement in light absorption is observed in these ranges (Figure S3). It is also notable that, at high particle densities (>0.60 wt %), light absorption rapidly increases at longer wavelengths, which may be attributable to aggregation of the nanostructures in the photoanodes, which results in the red-shift of the plasmon resonance to longer wavelengths.[11]
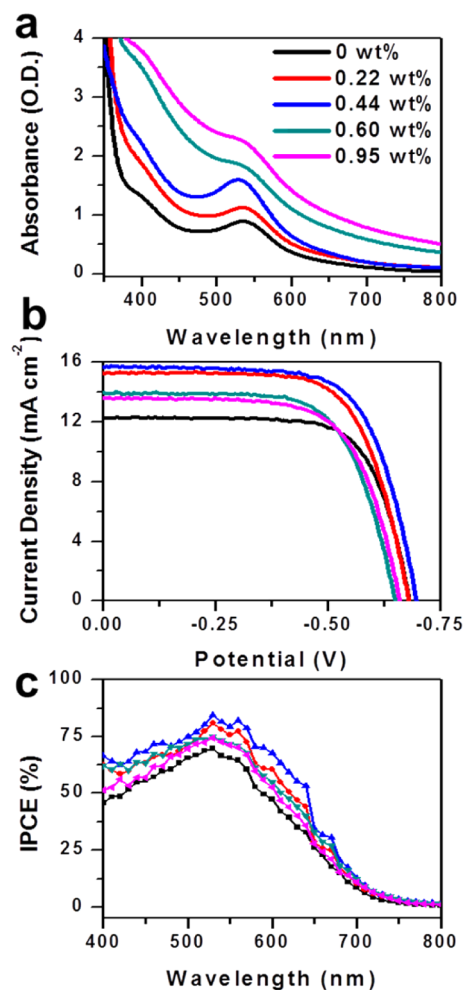
The power conversion efficiencies (PCEs) of reference and plasmon-enhanced DSSCs of equivalent area of 0.12 cm^2 were examined under AM 1.5 simulated solar light with each device being illuminated at 100 mW/cm^2 of power. Photocurrent spectra of the best performing DSSCs (Figure 3b) demonstrate that maximum plasmonic enhancement is achieved for DSSCs containing 0.44 wt % $Au/Ag/SiO_2$ nanostructures reaching a maximum PCE of 7.51%, which is 26% higher than the 5.97% PCE achieved with the reference DSSC. The spectral responses of the DSSCs were further investigated with IPCE measurements obtained with a supercontinuum white light laser coupled with an acousto-optic tunable filter used to modulate the wavelengths from 400 to 800 nm. Similar to the trend observed in absorbance spectra, the IPCE for the plasmon enhanced devices (Figure 3c) show an increase in photocurrent generation throughout the visible spectrum, with the maximum IPCE enhancements observed for the DSSCs incorporated with 0.44 wt % $Au/Ag/SiO_2$ NSs. Note that all plasmon-enhanced devices show an increase in photocurrent over the entire visible spectrum, corresponding well with the plasmon resonance of the nanostructures (Figure 1d).
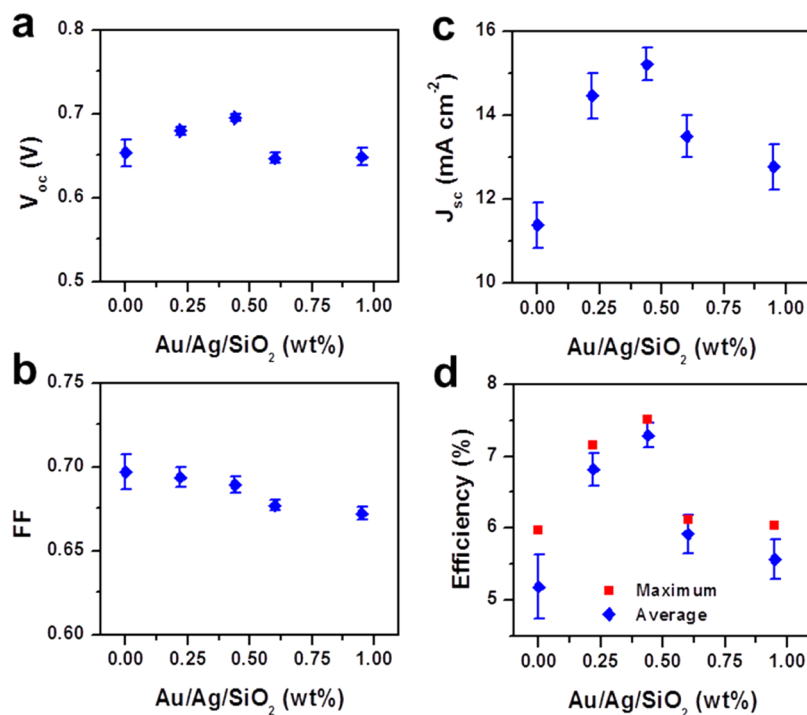
Figure 4. Average (a) open-circuit voltage, (b) fill factor, and (c) short circuit current density values for devices as a function of $Au/Ag/SiO_2$ nanostructure particle density (wt %). (d) Both best and average power conversion efficiencies obtained from five devices at each concentration tested.

The detailed device performance for both reference and nanostructure-incorporated DSSCs as a function of particle density is demonstrated in Figure 4, with the values shown in Table S1; we tested a total of five devices for each sample and used standard deviations from these devices to calculate uncertainties. The open-circuit voltages (V_{oc}) displays a slight increasing trend up to 0.44 wt % $Au/Ag/SiO_2$ NSs (Figure 4a), which is most likely attributed to improved charge transfer at optimal nanostructure loadings. Previous studies have performed impedance spectroscopy on plasmon-enhanced DSSC systems and reported a decrease in R_1, which is the charge transfer resistance over the conducting layer/photoanode interface and counter electrode/electrolyte interface collectively. This charge transfer resistance in the presence of metal nanoparticles is manifested in device performance, both as an increase in J_{sc} as well as V_{oc}.[56,57] It has also been reported that at high nanoparticle loadings R_2, the charge transfer resistance at the photoanode/electrolyte interface, increases, indicating that metal nanoparticles act as recombination centers. Therefore, optimizing the nanostructure concentrations in solar devices is of utmost importance.[27,58] A slight decrease in V_{oc} is observed at higher particle densities; as the V_{oc} is determined by the energy difference between the semiconductor under illumination and the Nerst potential of the I^-/I_3^- redox couple in the electrolyte, it is likely that the presence of metal nanostructures within the TiO_2 semiconductor results in a downshift in the Fermi level.[59,60] This downshift likely decreases the gap between the Fermi level of TiO_2 and the Nerst potential of the redox couple, which would decrease the V_{oc}.[33,61] At low particle densities, up to 0.44 wt % $Au/Ag/SiO_2$ NSs, the amount of metal present does not have appreciable effects on the Fermi level; therefore, this trend is observable when devices contain higher concentrations of $Au/Ag/SiO_2$ NSs. The fill factor (FF, Figure 4b) also has a consistent slight

decrease with increasing nanostructure concentrations suggesting that, at high densities, aggregation of nanostructures may result in electron trapping within metallic junctions.

The short circuit current density (J_{sc}) and PCE of the devices (Figure 4c,d) show a near-identical trend where the highest J_{sc} of 15.70 mA cm^{-2} and PCE of 7.51% are achieved at 0.44 wt % of $Au/Ag/SiO_2$ NSs. The maximum J_{sc} observed for the best-performing, plasmon-enhanced devices is 28% higher than the J_{sc} for the best-performing reference DSSC (12.27 mA cm^{-2}), analogous to the maximum enhancement achieved in PCE (26%). Since J_{sc} is reflective of the light harvesting capability of the devices, the trends in PCE and J_{sc} suggest plasmonic enhancement in DSSCs is contributed by increase in light absorption with minimal alterations in the electrochemical properties of the devices. The improved light harvesting in the nanostructure-incorporated devices can be attributed to (i) near-field coupling between the LSPR and adjacent sensitizer molecules, (ii) PRET from nanostructures to semiconductor, and (iii) light scattering in the nanoparticle far field, which can be trapped in the mesoporous semiconductor layer. These mechanisms are supported by the trends observed in absorption and IPCE measurements of the photoanodes. Due to the homogeneous mixing of the bimetallic nanostructures throughout the active layer (see Figure S1), we anticipate interparticle coupling between adjacent nanostructures may promote long-range surface plasmon polariton modes, which would also contribute to the overall enhancements. It is unlikely that hot electron transfer plays a role in our system due to the large size of the nanostructures and the ∼5 nm silica layer surrounding the Au/Ag-NSs. The process of hot electron generation in metal nanostructures depends on both the mean free path of electrons (λ_e) and thickness of insulating barrier between the metal and semiconductor. The λ_e in both Au and Ag is on the range of 40−50 nm;[62] as the size of both the
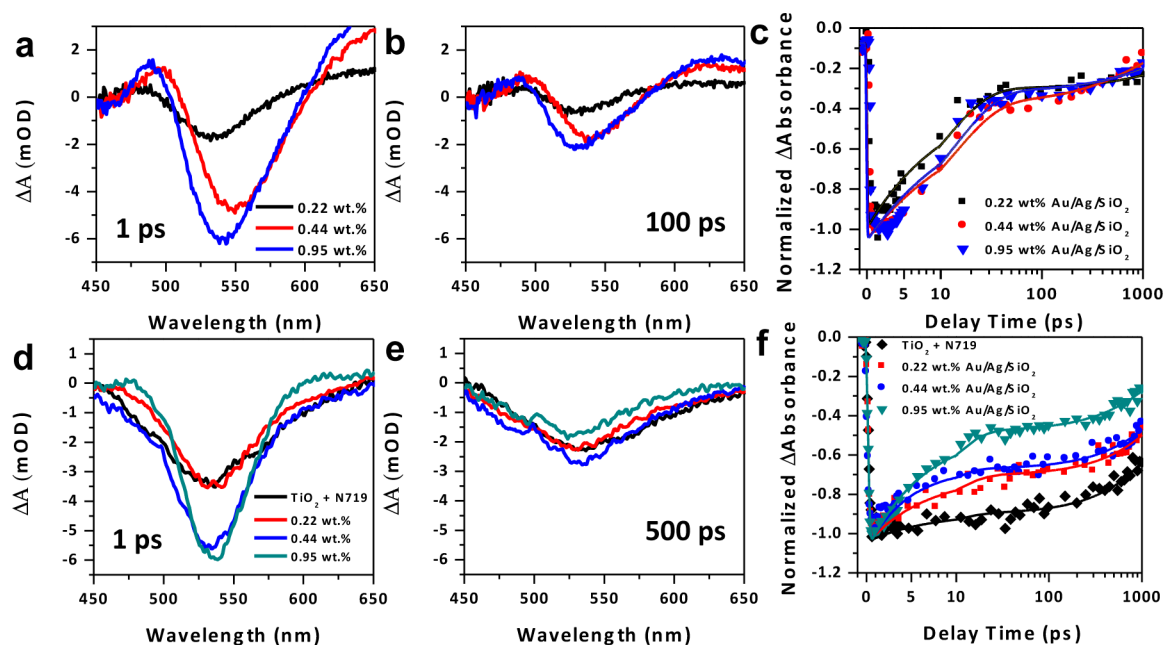
Figure 5. Transient absorption spectra for Au/Ag/SiO$_2$ + TiO$_2$ only samples (not sensitized with N719) at (a) 1 ps and (b) 100 ps time delays at the photobleaching state at ~530 nm. (c) Decay kinetics at 530 nm for all samples. Transient absorption spectra for N719 sensitized reference and N719 sensitized Au/Ag/SiO$_2$ NSs incorporated samples at (d) 1 ps and (e) 500 ps time delays at 530 nm. (f) Decay kinetics at 530 nm for the N719 sensitized reference and N719 sensitized plasmon-enhanced samples. All decay kinetics are shown with experimental data (symbols) fitted with a biexponential decay function (smooth line). Early time scales are plotted linearly; later time scales (>10 ps) plotted on a logarithmic scale with a base of 10.

nanocubes and the nanopyramids is >50 nm, fewer electrons likely travel to the metal surface due to loss of electrons by scattering. The few electrons that reach the metal/SiO$_2$ interface would then need to pass the insulating silica barrier. Since the electron tunneling barrier (Φ_b) of silica is ~3 nm or less[63−66] and the thickness of our spacer layer is ~5 nm, we do not anticipate that hot electrons transfer to the sensitizer or TiO$_2$.

We also observed a decrease in J_{sc} and PCE at high particle densities of Au/Ag/SiO$_2$ NSs. This decrease in performance is a consequence of excess metal which results in (*i*) a loss of absorbing dye volume due to the large volume of nanostructures, (*ii*) aggregation of nanostructures resulting in electron trapping within junctions, and (*iii*) nanostructure aggregation, which gives rise to interparticle coupling between adjacent nanostructures that results in electron−phonon coupling and subsequent generation of heat.[11,36,67] These detrimental processes would diminish the number of carriers available for photocurrent generation leading to decreased device performance.

To evaluate the fundamental mechanisms that drive plasmonic enhancement in DSSCs with Au/Ag/SiO$_2$ NSs, we performed TAS to understand dynamics of exciton generation, electron injection, and charge recombination within the mesoporous TiO$_2$ active layer. All samples were excited with a 400 nm pump and probed with white light continuum from 450 to 900 nm. We first examined the photoanodes in the absence of the sensitizer with the nanostructures embedded in the mesoporous TiO$_2$. Three different particle densities were chosen relevant to the plasmon-enhanced DSSCs tested earlier (see Figure 4), including 0.22, 0.44, and 0.95 wt % Au/Ag/SiO$_2$ NSs in TiO$_2$ (Note: DSSCs with 0.44 wt % Au/Ag/SiO$_2$ NSs were the best performing devices). The evolution of the TA spectra of the three samples at 1 and 100 ps time delays at 530

nm (Figure 5a,b) clearly demonstrate particle density dependent changes in spectral properties. The complete evolutionary spectra for the samples from 1−1000 ps time delays are provided in the SI (Figure S5a−c). The spectral feature observed at 530 nm for all samples is attributable to the photobleaching (PB) state of the plasmon mode of the Au/Ag/SiO$_2$ NSs which corresponds well with the 530 nm plasmon resonance of the bimetallic nanostructures (Figure 1d). The amplitude of the PB state increases monotonically with particle density at both 1 ps (Figure 5a) and 100 ps (Figure 5b) time delays, and the spectral evolution clearly shows the relaxation of the plasmon excitation culminates within the first 100 ps followed by energy transfer into TiO$_2$ conduction band. This is consistent with previous observation of inelastic electron−phonon scattering and subsequent energy transfer from metal nanoparticles to TiO$_2$ within the first 100 ps.[68] The decay kinetics of these samples were fit with a biexponential decay function (Figure 5c), and the corresponding amplitudes, time constants, and amplitude weighted lifetime, τ_{avg}, given by $\tau_{avg} = ((A_1 \times \tau_1 + A_2 \times \tau_2)/(A_1 + A_2))$, were derived from the fits and are shown in Table 1. We attribute the fast time constant (τ_1) to relaxation by means of electron−electron scattering after initial electronic excitation of nanostructures, which results in "hot" e$^-$ generation, and we attribute the slow time constant (τ_2) to energy transfer to TiO$_2$. Since τ_1 is relatively constant for all the samples, we infer "hot" electrons do not transfer across the insulating silica layer of the Au/Ag/SiO$_2$ NSs. However, the change in τ_2 among the samples and the overall rapid decrease in τ_{avg} with increasing particle density of Au/Ag/SiO$_2$ NSs is direct evidence of PRET. This suggests PRET occurs from the bimetallic nanostructures to the TiO$_2$ conduction band across the insulating SiO$_2$ layer resulting from the dipole−dipole relaxation of the excited plasmons.[28,68] We also note that energy transport between adjacent

Table 1. Amplitudes (A), Time Constants (τ), and Amplitude Weighted Lifetimes (τ_{avg}) Derived from Biexponential Fits of the Transient Absorption Decay Function for the Different Samples[a]

sample	A_1	τ_1 (ps)	A_2	τ_2 (ps)	τ_{avg} (ps)
0.22 wt % Au/Ag/SiO$_2$	−0.69	11.08	−0.23	2387	711
0.44 wt % Au/Ag/SiO$_2$	−0.68	13.98	−0.30	912	291
0.95 wt % Au/Ag/SiO$_2$	−0.74	13.86	−0.24	1553	392
TiO$_2$ + N719	−0.14	6.67	−0.90	2915	2523
0.22 wt % Au/Ag/SiO$_2$ + N719	−0.34	6.67	−0.70	2928	1977
0.44 wt % Au/Ag/SiO$_2$ + N719	−0.40	4.57	−0.67	2826	1781
0.95 wt % Au/Ag/SiO$_2$ + N719	−0.60	6.33	−0.48	1822	815

[a]All samples are embedded in mesoporous TiO$_2$.

nanostructures at high concentrations is possible and has been reported previously in metal nanoparticle chains.[69,70] However, at high concentrations, when nanostructures are touching, such long-range energy transfer will likely be a slower process relative to PRET from metal to TiO$_2$. Therefore, the latter mechanism will likely dominate. Further, previous studies have shown energy transfer from metal to TiO$_2$ when pumped at wavelengths higher than the bandgap of TiO$_2$ but lower or equivalent to the plasmon resonance of the metal.[71,72] With increasing concentration of Au/Ag/SiO$_2$ NSs in the mesoporous TiO$_2$ layer, an enhancement in plasmonic excitations is anticipated, which augments the rate of energy transfer and decreases τ_{avg}. Though, a slight increase in τ_{avg} is observable for the photoanode integrated with highest particle density, 0.95 wt %, Au/Ag/SiO$_2$ NSs. This is likely attributable to aggregation of Au/Ag/SiO$_2$ NSs in the mesoporous TiO$_2$ at such high concentrations, which results in damping of the plasmon resonance giving rise to a weaker PRET mechanism, and, therefore, an increase in the corresponding τ_{avg}. In addition to the PB state, we also observe broad photoinduced absorption (PIA) band at ∼650 nm (Figure S5a–d), which rapidly decays within the first 20−100 ps (Figure S5d,e), corresponding well with the 615 nm plasmon resonance peak of the Au/Ag/SiO$_2$ NSs. The PIA band is much weaker than the PB band; therefore, meaningful lifetimes could not be derived from the biexponential fits of the evolutionary spectra of the samples (Figure S5f). However, a particle density dependent trend is still observable, showing evidence of PRET from the Au/Ag/SiO$_2$ NSs into TiO$_2$.

We then investigated the photoanodes sensitized with N719 dye and compared the TA evolutionary spectra of the reference and plasmon-enhanced photoanodes at 530 nm (Figure 5d). Due to the strong spectral overlap in the extinction of the bimetallic nanostructures and N719 dye (see Figure 1d), the plasmon-enhanced samples are expected to have contributions from both the photobleaching of the dye and relaxation of the Au/Ag/SiO$_2$ NSs plasmons at 530 nm. Representative TA spectra at 1 and 500 ps of reference (TiO$_2$ + N719) and photoanodes embedded with nanostructures sensitized with N719 are shown in Figure 5d,e (full spectra of each sample for a range of time delays can be found in Figure S6). The spectra show a clear particle density-dependent evolution and complete recovery of the photobleaching state by 500 ps in all samples. The data were fit with a biexponential decay function, and corresponding amplitudes and lifetimes were derived (Table 1).

The fits yield a fast (τ_1) and a slow time constant (τ_2). Previous studies on N719-sensitized TiO$_2$ systems have demonstrated two time components; τ_1 was attributed to electron injection into the conduction band of the TiO$_2$ from the singlet metal to ligand charge transfer (^{1}MLCT) states and τ_2 to the triplet (^{3}MLCT) states of the excited N719 complexes.[73,74] The decay kinetics at 530 nm of the reference and plasmon-enhanced samples (Figure 5f) show several noteworthy characteristics: (*i*) the amplitude of the decay kinetics is enhanced for the nanostructure embedded photoanodes relative to the reference and monotonically increases with particle density. This is likely attributable to the stronger molecular absorption coefficient of metal nanostructures, typically on the order of 10^9 to 10^{10} M^{-1} cm^{-1},[35,75] as compared to N719, which is 1.58×10^4 M^{-1} cm^{-1}.[76] This suggests that the photobleaching of the excited Au/Ag/SiO$_2$ NSs is anticipated to be stronger than that of the dye alone. (*ii*) The amplitude-weighted lifetime, τ_{avg}, drastically decreases with increasing particle density relative to the reference sample. This suggests bimetallic nanostructures augment light trapping in the active layer of DSSCs enhancing the e$^-$/h$^+$ pairs generated in N719, resulting in more electrons being available to rapidly transfer to the TiO$_2$ conduction band. Therefore, the presence of metal nanostructures leads to faster electron injection into TiO$_2$ conduction band before recombination can occur in the bulk, resulting in shorter exciton lifetime. Decreased lifetime of photogenerated carriers in the presence of metal nanoparticles was recently reported in perovskite solar cells as well.[77] Finally, (*iii*) for the best performing plasmonic photoanodes embedded with 0.44 wt % Au/Ag/SiO$_2$ NSs, both the fast (τ_1) and slow time component (τ_2) are shorter relative to the reference photoanode (see Table 1). This is notable since the non-optimized concentrations (0.22 and 0.95 wt %) only affect electron dynamics at longer time scales (τ_2). These time constants indicate, following photoexcitation and plasmon enhanced light trapping in samples, PRET occurs at time scales of several hundred picoseconds, altering τ_2 across all samples. However, at the optimum particle density of 0.44 wt % Au/Ag/SiO$_2$ NSs, a strong metal−molecule interaction occurs via both plasmonic near-field and far-field coupling which likely populates the singlet (^{1}MLCT) states of the excited N719 molecules, promoting enhanced e$^-$/h$^+$ pair generation and rapid charge transfer into TiO$_2$. This phenomenon decreases τ_1 from 6.67 ps in reference to 4.57 ps in Au/Ag/SiO$_2$ NSs embedded photoanodes. We do observe τ_{avg} for the sensitized photoanodes decreases consistently with increasing particle density, but before sensitization, τ_{avg} slightly increases for the highest particle density (0.95 wt %). We anticipate this likely results from an improved charge transfer and PRET when the dye molecules surround the nanostructures; however, the exact mechanism of this observation remains unclear and further studies are underway. We note that a more in-depth study comparing various silica layer thicknesses will be interesting to understand the effect of PRET and will be performed in our follow up work. But to demonstrate that the thickness of the silica layer does have an impact on DSSCs electron dynamics, we have also performed TAS on Au/Ag nanostructures coated with 30 nm thick SiO$_2$ layer and embedded in DSSC photoanodes (Figures S7 and S8). A detailed discussion is provided in the Supporting Information.

In summary, we investigated the impact of shape- and composition-controlled Au/Ag/SiO$_2$ core/shell/shell bimetallic nanostructures on the device performance and electron

dynamics of DSSCs. The best performing plasmon-enhanced DSSCs resulted in 7.51% PCE relative to 5.97% for reference DSSCs, giving rise to ~26% enhancement. By varying the particle density, a systematic dependence of device performance on nanostructure concentration was observed. Maximum enhancement was achieved at 0.44 wt % Au/Ag/SiO$_2$ NSs, which is substantially less than previously studied DSSCs integrated with monometallic nanostructures and poorly controlled shapes. Enhanced device performance was attributed to increased light harvesting enabled by the intense near-field interactions of nanostructures with N719, far-field coupling of scattered light into the active layer, and PRET from nanostructures to TiO$_2$. Transient absorption spectroscopy studies demonstrated a decrease in amplitude weighted lifetimes with increasing particle density, showing strong evidence of PRET. Further, unlike the unoptimized plasmonic devices (0.22 wt %, 0.95 wt %), which only impact the slow time constants, plasmonic DSSCs with optimized particle density of Au/Ag/SiO$_2$ NSs (0.44 wt %) alter both the fast and slow lifetimes. We attributed this to strong metal−molecule interaction that likely populates the singlet metal ligand charge transfer states of the excited dye, augmenting e$^-$/h$^+$ pair generation and rapid charge transfer into TiO$_2$. We anticipate morphology-controlled bimetallic nanostructures can be ultimately tailored, tuned, and targeted toward a range of optical and optoelectronic technologies beyond DSSCs.

METHODS

Detailed experimental methods are provided in the Supporting Information.

ASSOCIATED CONTENT

Ⓢ Supporting Information

The Supporting Information is available free of charge on the ACS Publications website at DOI: 10.1021/acsphotonics.5b00552.

Detailed experimental procedures and additional transient absorption spectroscopy data are provided (PDF).

AUTHOR INFORMATION

Corresponding Author
*E-mail: rizia.bardhan@vanderbilt.edu.

Notes

The authors declare no competing financial interest.

ACKNOWLEDGMENTS

REFERENCES

(1) Wu, W.-Q.; Xu, Y.-F.; Su, C.-Y.; Kuang, D.-B. Ultra-long anatase TiO$_2$ nanowire arrays with multi-layered configuration on FTO glass for high-efficiency dye-sensitized solar cells. *Energy Environ. Sci.* **2014**, *7*, 644−649.

(2) Margulis, G. Y.; Christoforo, M. G.; Lam, D.; Beiley, Z. M.; Bowring, A. R.; Bailie, C. D.; Salleo, A.; McGehee, M. D. Spray Deposition of Silver Nanowire Electrodes for Semitransparent Solid-State Dye-Sensitized Solar Cells. *Adv. Energy Mater.* **2013**, *3*, 1657−1663.

(3) Erwin, W. R.; Oakes, L.; Chatterjee, S.; Zarick, H. F.; Pint, C. L.; Bardhan, R. Engineered Porous Silicon Counter Electrodes for High Efficiency Dye-Sensitized Solar Cells. *ACS Appl. Mater. Interfaces* **2014**, *6*, 9904−9910.

(4) Yen, Y. C.; Chen, P. H.; Chen, J. Z.; Chen, J. A.; Lin, K. J. Plasmon-induced efficiency enhancement on dye-sensitized solar cell by a 3D TNW-AuNP layer. *ACS Appl. Mater. Interfaces* **2015**, *7*, 1892−1898.

(5) Winans, J. D.; Hungerford, C.; Shome, K.; Rothberg, L. J.; Fauchet, P. M. Plasmonic effects in ultrathin amorphous silicon solar cells: performance improvements with Ag nanoparticles on the front, the back, and both. *Opt. Express* **2015**, *23*, A92−A105.

(6) Sha, W. E.; Li, X.; Choy, W. C. Breaking the space charge limit in organic solar cells by a novel plasmonic-electrical concept. *Sci. Rep.* **2014**, *4*, 6236.

(7) Lee, D. H.; Kwon, J. Y.; Maldonado, S.; Tuteja, A.; Boukai, A. Extreme light absorption by multiple plasmonic layers on upgraded metallurgical grade silicon solar cells. *Nano Lett.* **2014**, *14*, 1961−1967.

(8) Ding, I. K.; Zhu, J.; Cai, W.; Moon, S.-J.; Cai, N.; Wang, P.; Zakeeruddin, S. M.; Grätzel, M.; Brongersma, M. L.; Cui, Y.; McGehee, M. D. Plasmonic Dye-Sensitized Solar Cells. *Adv. Energy Mater.* **2011**, *1*, 52−57.

(9) Ding, B.; Lee, B. J.; Yang, M.; Jung, H. S.; Lee, J.-K. Surface-Plasmon Assisted Energy Conversion in Dye-Sensitized Solar Cells. *Adv. Energy Mater.* **2011**, *1*, 415−421.

(10) Baek, S.-W.; Park, G.; Noh, J.; Cho, C.; Lee, C.-H.; Seo, M.-K.; Song, H.; Lee, J.-Y. Au@Ag Core-Shell Nanocubes for Efficient Plasmonic Light Scattering Effect in Low Bandgap Organic Solar Cells. *ACS Nano* **2014**, *8*, 3302−3312.

(11) Zarick, H. F.; Hurd, O.; Webb, J. A.; Hungerford, C.; Erwin, W. R.; Bardhan, R. Enhanced Efficiency in Dye-Sensitized Solar Cells with Shape-Controlled Plasmonic Nanostructures. *ACS Photonics* **2014**, *1*, 806−811.

(12) Webb, J. A.; Erwin, W. R.; Zarick, H. F.; Aufrecht, J.; Manning, H. W.; Lang, M. J.; Pint, C. L.; Bardhan, R. Geometry-Dependent Plasmonic Tunability and Photothermal Characteristics of Multi-branched Gold Nanoantennas. *J. Phys. Chem. C* **2014**, *118*, 3696−3707.

(13) Linic, S.; Aslam, U.; Boerigter, C.; Morabito, M. Photochemical transformations on plasmonic metal nanoparticles. *Nat. Mater.* **2015**, *14*, 567−576.

(14) Sonntag, M. D.; Klingsporn, J. M.; Zrimsek, A. B.; Sharma, B.; Ruvuna, L. K.; Van Duyne, R. P. Molecular plasmonics for nanoscale spectroscopy. *Chem. Soc. Rev.* **2014**, *43*, 1230−1247.

(15) Adato, R.; Altug, H. In-situ ultra-sensitive infrared absorption spectroscopy of biomolecule interactions in real time with plasmonic nanoantennas. *Nat. Commun.* **2013**, *4*, 2154.

(16) Webb, J. A.; Aufrecht, J.; Hungerford, C.; Bardhan, R. Ultrasensitive analyte detection with plasmonic paper dipsticks and swabs integrated with branched nanoantennas. *J. Mater. Chem. C* **2014**, *2*, 10446−10454.

(17) Webb, J. A.; Bardhan, R. Emerging advances in nanomedicine with engineered gold nanostructures. *Nanoscale* **2014**, *6*, 2502−2530.

(18) Gandra, N.; Portz, C.; Nergiz, S. Z.; Fales, A.; Vo-Dinh, T.; Singamaneni, S. Inherently stealthy and highly tumor-selective gold nanoraspberries for photothermal cancer therapy. *Sci. Rep.* **2015**, *5*, 10311.

(19) Meir, R.; Shamalov, K.; Betzer, O.; Motiei, M.; Horovitz-Fried, M.; Yehuda, R.; Popovtzer, A.; Popovtzer, R.; Cohen, C. J. Nanomedicine for Cancer Immunotherapy: Tracking Cancer-Specific T-Cells in Vivo with Gold Nanoparticles and CT Imaging. *ACS Nano* **2015**, *9*, 6363−6372.

(20) Xu, Q.; Liu, F.; Liu, Y.; Cui, K.; Feng, X.; Zhang, W.; Huang, Y. Broadband light absorption enhancement in dye-sensitized solar cells with Au-Ag alloy popcorn nanoparticles. *Sci. Rep.* **2013**, *3*, 2112.

(21) Hägglund, C.; Zäch, M.; Kasemo, B. Enhanced charge carrier generation in dye sensitized solar cells by nanoparticle plasmons. *Appl. Phys. Lett.* **2008**, *92*, 013113.

(22) Atwater, H. A.; Polman, A. Plasmonics for Improved Photovoltaic Devices. *Nat. Mater.* **2010**, *9*, 205−213.

(23) Mukherjee, S.; Libisch, F.; Large, N.; Neumann, O.; Brown, L. V.; Cheng, J.; Lassiter, J. B.; Carter, E. A.; Nordlander, P.; Halas, N. J. Hot electrons do the impossible: plasmon-induced dissociation of H$_2$ on Au. *Nano Lett.* **2013**, *13*, 240−247.

(24) van Lare, M. C.; Polman, A. Optimized Scattering Power Spectral Density of Photovoltaic Light-Trapping Patterns. *ACS Photonics* **2015**, *2*, 822−831.

(25) Zhou, N.; Lopez-Puente, V.; Wang, Q.; Polavarapu, L.; Pastoriza-Santos, I.; Xu, Q.-H. Plasmon-enhanced light harvesting: applications in enhanced photocatalysis, photodynamic therapy and photovoltaics. *RSC Adv.* **2015**, *5*, 29076−29097.

(26) Gangishetty, M. K.; Lee, K. E.; Scott, R. W.; Kelly, T. L. Plasmonic Enhancement of Dye Sensitized Solar Cells in the Red-to-near-Infrared Region using Triangular Core-Shell Ag@SiO$_2$ Nanoparticles. *ACS Appl. Mater. Interfaces* **2013**, *5*, 11044−11051.

(27) Chang, S.; Li, Q.; Xiao, X.; Wong, K. Y.; Chen, T. Enhancement of low energy sunlight harvesting in dye-sensitized solar cells using plasmonic gold nanorods. *Energy Environ. Sci.* **2012**, *5*, 9444−9448.

(28) Cushing, S. K.; Li, J.; Meng, F.; Senty, T. R.; Suri, S.; Zhi, M.; Li, M.; Bristow, A. D.; Wu, N. Photocatalytic activity enhanced by plasmonic resonant energy transfer from metal to semiconductor. *J. Am. Chem. Soc.* **2012**, *134*, 15033−15041.

(29) Cushing, S. K.; Li, J.; Bright, J.; Yost, B. T.; Zheng, P.; Bristow, A. D.; Wu, N. Controlling Plasmon-Induced Resonance Energy Transfer and Hot Electron Injection Processes in Metal@TiO2Core−Shell Nanoparticles. *J. Phys. Chem. C* **2015**, *119*, 16239−16244.

(30) Schuck, P. J. Hot electrons go through the barrier. *Nat. Nanotechnol.* **2013**, *8*, 799−800.

(31) Wang, F.; Melosh, N. A. Power-independent wavelength determination by hot carrier collection in metal-insulator-metal devices. *Nat. Commun.* **2013**, *4*, 1711.

(32) Sheehan, S. W.; Noh, H.; Brudvig, G. W.; Cao, H.; Schmuttenmaer, C. A. Plasmonic Enhancement of Dye-Sensitized Solar Cells Using Core−Shell−Shell Nanostructures. *J. Phys. Chem. C* **2013**, *117*, 927−934.

(33) Jang, Y. H.; Jang, Y. J.; Kochuveedu, S. T.; Byun, M.; Lin, Z.; Kim, D. H. Plasmonic dye-sensitized solar cells incorporated with Au-TiO(2) nanostructures with tailored configurations. *Nanoscale* **2014**, *6*, 1823−1832.

(34) Dang, X.; Qi, J.; Klug, M. T.; Chen, P. Y.; Yun, D. S.; Fang, N. X.; Hammond, P. T.; Belcher, A. M. Tunable localized surface plasmon-enabled broadband light-harvesting enhancement for high-efficiency panchromatic dye-sensitized solar cells. *Nano Lett.* **2013**, *13*, 637−642.

(35) Brown, M. D.; Suteewong, T.; Kumar, R. S.; D'Innocenzo, V.; Petrozza, A.; Lee, M. M.; Wiesner, U.; Snaith, H. J. Plasmonic dye-sensitized solar cells using core-shell metal-insulator nanoparticles. *Nano Lett.* **2011**, *11*, 438−445.

(36) Qi, J.; Dang, X.; Hammond, P. T.; Belcher, A. M. Highly efficient plasmon-enhanced dye-sensitized solar cells through metal@oxide core-shell nanostructure. *ACS Nano* **2011**, *5*, 7108−7116.

(37) Halas, N. J.; Lal, S.; Chang, W. S.; Link, S.; Nordlander, P. Plasmons in strongly coupled metallic nanostructures. *Chem. Rev.* **2011**, *111*, 3913−3961.

(38) Grady, N. K.; Halas, N. J.; Nordlander, P. Influence of dielectric function properties on the optical response of plasmon resonant metallic nanoparticles. *Chem. Phys. Lett.* **2004**, *399*, 167−171.

(39) Xu, Q.; Liu, F.; Liu, Y.; Meng, W.; Cui, K.; Feng, X.; Zhang, W.; Huang, Y. Aluminum plasmonic nanoparticles enhanced dye sensitized solar cells. *Opt. Express* **2014**, *22*, A301−A310.

(40) Bai, L.; Li, M.; Guo, K.; Luoshan, M.; Mehnane, H. F.; Pei, L.; Pan, M.; Liao, L.; Zhao, X. Plasmonic enhancement of the performance of dye-sensitized solar cell by core−shell AuNRs@SiO2 in composite photoanode. *J. Power Sources* **2014**, *272*, 1100−1105.

(41) Hu, M.; Chen, J.; Li, Z. Y.; Au, L.; Hartland, G. V.; Li, X.; Marquez, M.; Xia, Y. Gold nanostructures: engineering their plasmonic properties for biomedical applications. *Chem. Soc. Rev.* **2006**, *35*, 1084−1094.

(42) Hu, M.; Petrova, H.; Wang, X.; Hartland, G. Time-Resolved and Steady State Spectroscopy of Polydisperse Colloidal Silver Nanoparticle Samples. *J. Phys. Chem. B* **2005**, *109*, 14426−14432.

(43) Sharma, V.; Park, K.; Srinivasarao, M. Colloidal dispersion of gold nanorods: Historical background, optical properties, seed-mediated synthesis, shape separation and self-assembly. *Mater. Sci. Eng., R* **2009**, *65*, 1−38.

(44) Torngren, B.; Akitsu, K.; Ylinen, A.; Sanden, S.; Jiang, H.; Ruokolainen, J.; Komatsu, M.; Hamamura, T.; Nakazaki, J.; Kubo, T.; Segawa, H.; Osterbacka, R.; Smatt, J. H. Investigation of plasmonic gold-silica core-shell nanoparticle stability in dye-sensitized solar cell applications. *J. Colloid Interface Sci.* **2014**, *427*, 54−61.

(45) Adhyaksa, G. W.; Baek, S. W.; Lee, G. I.; Lee, D. K.; Lee, J. Y.; Kang, J. K. Coupled near- and far-field scattering in silver nanoparticles for high-efficiency, stable, and thin plasmonic dye-sensitized solar cells. *ChemSusChem* **2014**, *7*, 2461−2468.

(46) Standridge, S.; Schatz, G. C.; Hupp, J. T. Distance Dependence of Plasmon-Enhanced Photocurrent in Dye-Sensitized Solar Cells. *J. Am. Chem. Soc.* **2009**, *131*, 8407−8409.

(47) Kalaignan, G.; Kang, Y. A review on mass transport in dye-sensitized nanocrystalline solar cells. *J. Photochem. Photobiol., C* **2006**, *7*, 17−22.

(48) Aouani, H.; Mahboub, O.; Devaux, E.; Rigneault, H.; Ebbesen, T. W.; Wenger, J. Plasmonic antennas for directional sorting of fluorescence emission. *Nano Lett.* **2011**, *11*, 2400−2406.

(49) Bardhan, R.; Grady, N. K.; Cole, J. R.; Joshi, A.; Halas, N. J. Fluorescence Enhancement by Au Nanostructures: Nanoshells and Nanorods. *ACS Nano* **2009**, *3*, 744−752.

(50) Dong, H.; Wu, Z.; El-Shafei, A.; Xia, B.; Xi, J.; Ning, S.; Jiao, B. Ag-encapsulated Au plasmonic nanorods for enhnaced for enhanced dye-sensitized solar cell performance. *J. Mater. Chem. A* **2015**, *3*, 4659−4668.

(51) Liu, J.-H.; Wang, A.-Q.; Chi, Y.-S.; Lin, H.-P.; Mou, C.-Y. Synergistic Effect in an Au−Ag Alloy Nanocatalyst: CO Oxidation. *J. Phys. Chem. B* **2005**, *109*, 40−43.

(52) Polavarapu, L.; Mourdikoudis, S.; Pastoriza-Santos, I.; Pérez-Juste, J. Nanocrystal engineering of noble metals and metal chalcogenides: controlling the morphology, composition and crystallinity. *CrystEngComm* **2015**, *17*, 3727−3762.

(53) Haggui, M.; Dridi, M.; Plain, J.; Marguet, S.; Perez, H.; Schatz, G. C.; Wiederrecht, G. P.; Gray, S. K.; Bachelot, R. Spatial Confinement of Electromagnetic Hot and Cold Spots in Gold Nanocubes. *ACS Nano* **2012**, *6*, 1299−1307.

(54) Rycenga, M.; Kim, M. H.; Camargo, P. H. C.; Cobley, C.; Li, Z.-Y.; Xia, Y. Surface-Enhanced Raman Scattering: Comparison of Three Different Molecules on Single-Crystal Nanocubes and Nanospheres of Silver. *J. Phys. Chem. A* **2009**, *113*, 3932−3939.

(55) Rycenga, M.; Xia, X.; Moran, C. H.; Zhou, F.; Qin, D.; Li, Z. Y.; Xia, Y. Generation of hot spots with silver nanocubes for single-molecule detection by surface-enhanced Raman scattering. *Angew. Chem., Int. Ed.* **2011**, *50*, 5473−5477.

(56) Muduli, S.; Game, O.; Dhas, V.; Vijayamohanan, K.; Bogle, K. A.; Valanoor, N.; Ogale, S. B. TiO$_2$−Au plasmonic nanocomposite for enhanced dye-sensitized solar cell (DSSC) performance. *Sol. Energy* **2012**, *86*, 1428−1434.

(57) Liu, Y.; Zhai, H.; Guo, F.; Huang, N.; Sun, W.; Bu, C.; Peng, T.; Yuan, J.; Zhao, X. Synergistic effect of surface plasmon resonance and constructed hierarchical TiO$_2$ spheres for dye-sensitized solar cells. *Nanoscale* **2012**, *4*, 6863−6869.

(58) Guo, K.; Li, M.; Fang, X.; Liu, X.; Sebo, B.; Zhu, Y.; Hu, Z.; Zhao, X. Preparation and enhanced properties of dye-sensitized solar

cells by surface plasmon resonance of Ag nanoparticles in nano-composite photoanode. *J. Power Sources* **2013**, *230*, 155−160.

(59) Kumar, P. N.; Deepa, M.; Srivastava, A. K. Ag plasmonic nanostructures and a novel gel electrolyte in high efficiency TiO_2/CdS solar cell. *Phys. Chem. Chem. Phys.* **2015**, *17*, 10040−10052.

(60) Kumar, P. N.; Deepa, M.; Ghosal, P. Low-Cost Copper Nanostructures Impart High Efficiencies to Quantum Dot Solar Cells. *ACS Appl. Mater. Interfaces* **2015**, *7*, 13303−13313.

(61) Du, J.; Qi, J.; Wang, D.; Tang, Z. Facile synthesis of Au@TiO_2 core−shell hollow spheres for dye-sensitized solar cells with remarkably improved efficiency. *Energy Environ. Sci.* **2012**, *5*, 6914−6918.

(62) Link, S.; El-Sayed, M. A. Shape and size dependence of radiative, non-radiative and photothermal properties of gold nanocrystals. *Int. Rev. Phys. Chem.* **2000**, *19*, 409−453.

(63) Deal, B. E.; Snow, E. H. Barrier Energies in Metal-Silicon Dioxide-Silicon Structures. *J. Phys. Chem. Solids* **1966**, *27*, 1873−1879.

(64) Lee, W. C.; Hu, C. Modeling CMOS Tunneling Currents Through Ultrathin Gate Oxide Due to Conduction- and Valence-Band Electron and Hole Tunneling. *IEEE Trans. Electron Devices* **2001**, *48*, 1366−1373.

(65) Lin, C. H.; Liu, C. W. Metal-insulator-semiconductor photo-detectors. *Sensors* **2010**, *10*, 8797−8826.

(66) Weinberg, Z. A.; Hartstein, A. Photon Assisted Tunneling from Aluminum to Silicon Dioxide. *Solid State Commun.* **1976**, *20*, 179−182.

(67) Kim, H.-Y.; Suh, J. S. Panchromatic quasi-monolayer of Ag nanoparticles for high efficiency dye-sensitized solar cells. *RSC Adv.* **2015**, *5*, 59895−59902.

(68) Du, L.; Furube, A.; Yamamoto, K.; Hara, K.; Katoh, R.; Tachiya, M. Plasmon-Induced Charge Separation and Recombination Dynamics in Gold-TiO2 Nanoparticle Systems: Dependence on TiO_2 Particle Size. *J. Phys. Chem. C* **2009**, *113*, 6454−6462.

(69) Willingham, B.; Link, S. Energy transport in metal nanoparticle chains via sub-radiant plasmon modes. *Opt. Express* **2011**, *19*, 6450−6461.

(70) Solis, D.; Willingham, B.; Nauert, S. L.; Slaughter, L. S.; Olson, J.; Swanglap, P.; Paul, A.; Chang, W.-S.; Link, S. Electromagnetic Energy Transport in Nanoparticle Chains via Dark Plasmon Modes. *Nano Lett.* **2012**, *12*, 1349−1353.

(71) Du, L.; Furube, A.; Hara, K.; Katoh, R.; Tachiya, M. Ultrafast plasmon induced electron injection mechanism in gold−TiO_2 nanoparticle system. *J. Photochem. Photobiol., C* **2013**, *15*, 21−30.

(72) Furube, A.; Du, L.; Hara, K.; Katoh, R.; Tachiya, M. Ultrafast Plasmon-Induced Electron Transfer from Gold Nanodots into TiO2 Nanoparticles. *J. Am. Chem. Soc.* **2007**, *129*, 14852−14853.

(73) Yu, L.-H.; Xi, J.-Y.; Lo, K. C.; Antrobus, L. J.; Phillips, D. L.; Chan, W. K. Transient Absorption of N719 and its Electron Transfer Kinetics on ZnO Nanoparticles Surface. *J. Inorg. Organomet. Polym. Mater.* **2015**, *25*, 169−175.

(74) Hsu, H.-Y.; Cheng, C.-W.; Huang, W.-K.; Lee, Y.-P.; Diau, E. W.-G. Femtosecond Infrared Transient Absorption Dynamics of Benzimidazole-Based Ruthenium Complexes on TiO_2 Films for Dye-Sensitized Solar Cells. *J. Phys. Chem. C* **2014**, *118*, 16904−16911.

(75) Cho, E. C.; Kim, C.; Zhou, F.; Cobley, C. M.; Song, K. H.; Chen, J.; Li, Z.-Y.; Wang, L. V.; Xia, Y. Measuring the Optical Absorption Cross Sections of Au−Ag Nanocages and Au Nanorods by Photoacoustic Imaging. *J. Phys. Chem. C* **2009**, *113*, 9023−9028.

(76) Kong, F.; Dai, S.; Wang, K. Purification of Bipyridyl Ruthenium Dye and Its Application in Dye-Sensitized Solar Cells. *Plasma Sci. Technol.* **2006**, *8*, 531−534.

(77) Lu, Z.; Pan, X.; Ma, Y.; Li, Y.; Zheng, L.; Zhang, D.; Xu, Q.; Chen, Z.; Wang, S.; Qu, B.; Liu, F.; Huang, Y.; Xiao, L.; Gong, Q. Plasmonic-enhanced perovskite solar cells using alloy popcorn nanoparticles. *RSC Adv.* **2015**, *5*, 11175−11179.